RESEARCH PAPER

Effect of the hybrid composition on the physicochemical properties and morphology of iron oxide–gold nanoparticles

C. M. Barnett · M. Gueorguieva · M. R. Lees ·
D. J. McGarvey · R. J. Darton · C. Hoskins

Abstract Hybrid nanoparticles (HNPs) formed from iron oxide cores and gold nano-shells are becoming increasingly applicable in biomedicine. However, little investigation has been carried out on the effects of the constituent components on their physical characteristics. Here we determine the effect of polymer intermediate, gold nano-shell thickness and magnetic iron oxide core diameter on the morphological and physical properties of these nano-hybrids. Our findings suggest that the use of polymer intermediate directly impacts the morphology of the nanostructure formed. Here, we observed the formation of nano-sphere and nano-star structures by varying the cationic polymer intermediate. The nano-stars formed have a larger magnetic coercivity, T_2 relaxivity and exhibited a unique characteristic nano-heating pattern upon laser irradiation. Increasing the iron oxide core diameter resulted in a greater T_2 relaxivity enhanced and nano-heating capabilities due to increased surface area. Increasing the gold nano-shell thickness resulted in a decreased efficiency as a nano-heater along with a decrease in T_2 relaxivity. These results highlight the importance of identifying the key traits required when fabricating HNPs in order to tailor them to specific applications.

C. M. Barnett
School of Pharmacy,
Keele University, Keele ST5 5BG, UK

M. Gueorguieva
Institute of Medical Science and Technology,
University of Dundee, Dundee DD2 1FD, UK

M. R. Lees
Physics Department, University of Warwick,
Coventry CV4 7AL, UK

D. J. McGarvey · R. J. Darton
Lennard-Jones Laboratories, School of Physical and
Geographical Sciences, Keele University, Keele ST5
5BG, UK

C. Hoskins (✉)
Institute of Science and Technology in Medicine,
Keele University, Keele ST5 5BG, UK
e-mail: c.hoskins@mema.keele.ac.uk

Introduction

Over the past decade metallic nanoparticles have been extensively studied for possible biomedical application (Bystrejewski et al. 2007; Thanh and Green 2010; Bhattacharya and Mukherjee 2008; Fadeel and Garcia-Bennett 2010; Guerrero-Martínez et al. 2011). Commonly, metal oxides such as copper oxide (Ren et al. 2009), iron oxide (Gupta and Gupta 2005),

aluminium oxide (Ansari and Hussain 2011) and zinc oxide (Ansari et al. 2011) have been reported. Metal nanoparticles require careful surface engineering before introduction into biological environments. Commonly, polymers were used to render these particles biocompatible (Thanh and Green 2010). However, studies have suggested that these flexible polymers cannot fully protect the metal oxide cores, resulting in degradation and leading to free radical release (Hoskins et al. 2012a). It is widely recognised that free radicals increase levels of cellular stress in some cases leading to cell death (Minotti and Aust 1987; Fraga et al. 1987). In fact in early 2012, Feridex® (the clinically used magnetic resonance imaging (MRI) contrast agent composed of dextran-coated iron oxide) was withdrawn from use in humans as a result of patients experiencing unpredictable side effects attributable to free radical production.

Modern advances in nanotechnology have led to alloy metallic nanoparticle formation. Alloy nanoparticles are particles formed with two or more substituent metallic components. For example, iron–platinum (FePt) particles have recently been reported which possess both the magnetic moment attributed to the iron atoms and potential anticancer activity due to the presence of the platinum moiety (Chen et al. 2012). The combination of metals with unique properties has resulted in multimodal particles with increased functionality.

Another class of nanoparticles containing two or more metallic substances are hybrid nanoparticles (HNPs). HNPs are composed of a metallic core coated by a shell of a different metal. Iron oxide–gold HNPs have recently been the focus of a number of investigations (Goon et al. 2009; Smolensky et al. 2011; Zhang et al. 2010). Here, magnetic iron oxide nanoparticles are coated with a gold shell (the presence of gold is advantageous over flexible polymer coatings due to its rigidity). The complete coat formed prevents degradation of the inner iron oxide core thus preventing free radical initiation by Fe^{3+} (Hoskins et al. 2012a). This increases the long-term safety profile of the nanoparticles. Colloidal gold is renowned for its unique surface plasmon resonance (SPR) property. SPR is a phenomenon whereby, when gold nanostructures are irradiated with photons of light at the appropriate wavelength, the light will become absorbed and scattered. This absorption rapidly converts the energy of the light to thermal energy and hence the particles heat up (Jain 2007). The amalgamation of magnetic and SPR properties in one nanoparticle holds great potential for biomedical applications. Such advances in image guided therapies facilitates knowledge-based treatments of diseases such as cancer. These include photo thermal drug delivery, image guided targeted delivery and image guided photo ablation (Ji et al. 2007).

Recently, a number of studies have reported the synthesis of iron oxide–gold HNPs (Smolensky et al. 2011; Zhang et al. 2010; Ji et al. 2007; Hoskins et al. 2012b). Previous investigations have shown the use of a polymer 'cushion' between the iron oxide core and the gold coating to be advantageous over direct gold coating of the magnetic core (Smolensky et al. 2011). This 'cushion' or spacer reportedly prevents gold migration into the core, maintaining the saturation magnetisation and relaxivity (Smolensky et al. 2011). However, previous work has been application driven and in-depth studies of how individual hybrid components affect overall performance is still lacking. The work reported here focuses on the effect of the iron oxide core diameter, type of polymer cushion and gold coating thickness on the physicochemical and morphological properties of the HNPs. The particles have been synthesised and fully characterised, and their thermal and magnetic properties (T_2 relaxivity and coercivity) evaluated. In general, there is no international agreement on the nanoscale range. In this study, we refer to particles between 1 and 300 nm as nanosized.

Materials and methods

All chemicals were purchased from Sigma-Aldrich (UK).

Synthesis of HNPs

Iron oxide cores were synthesised using a well-established precipitation reaction (Hoskins et al. 2012a; Andrés Vergés et al. 2008; Sugimoto and Matijević 1980). Reaction time was varied in order to produce particles of different diameter (8, 18 and 24 h). Briefly, sodium hydroxide (NaOH, 1.030 g) and potassium nitrate (KNO₃, 1.820 g) were dissolved in deionised water (H_2O, 180 mL) at 90 °C under nitrogen (N₂) for 1 h. Iron(III) sulphate heptahydrate

($FeSO_4 \cdot 7H_2O$, 3.89 g) was dissolved in sulphuric acid (H_2SO_4, 20 mL) and added to the reaction mixture with stirring for 12, 18 and 24 h at 90 °C. The reaction was cooled on ice and the particles were washed in H_2O (six times). The particles were magnetically separated from solution and resuspended in water. This aqueous solution (5 mL) was added to 20 mL of polymer aqueous solution (5 mg mL^{-1}, pH 9) and sonicated for 2 h. The polymers used to achieve different coatings were poly(L-lysine) (PLL, [$C_6H_{12}N_2O$]$_n$), poly(ethylenimine) (PEI, [C_2H_5N]$_n$) and poly(allylamine) (PAA, [$C3H_7N$)]$_n$), respectively. The particles were separated from solution using a high powered magnet followed by extensive washing with H_2O. The washed particles were resuspended in 5 mL of H_2O.

Polymer-coated nanoparticles (2 mL) were stirred in an aqueous solution containing 2 nm colloidal gold (90 mL). [Gold seeds were prepared by addition of chloroauric acid (HAuCl$_4$, 4 %, 375 μL) to 100 mL ice water with stirring. This was followed by addition of 0.2 M sodium carbonate (Na$_2$CO$_3$, 500 μL). After 5 min stirring sodium borohydride (NaBH$_4$, 0.5 mg mL^{-1}, 5 mL) was added slowly.] The Fe$_3$O$_4$-polymer solution and gold seeds were stirred at room temperature for 2 h. Particle separation from solution was followed by stabilisation stirring with 0.1 mg mL^{-1} PEI (MW 2000) for 10 min. Finally, the particles were washed before resuspending in 2 mL H_2O. Gold coating was achieved by reduction of HAuCl$_4$ onto the particle surface forming a complete shell (Goon et al. 2009). A solution of sodium hydroxide (NaOH, 0.01 M, 110 mL) was stirred with the particle solution. To this 0.5 mL of 1 % HAuCl$_4$ was added followed by hydroxyl amine (NH$_2$OH·HCl, 0.75 mL, 0.2 M). Consecutive iterative reductions were carried out by the addition of 1 % HAuCl$_4$ (0.5 mL) and 0.2 M NH$_2$OH·HCl (0.25 mL) with 10 min intervals (depending on shell thickness). The final solution was stirred for 0.5 h followed by washing (five times) in H_2O and magnetic separation from solution. The particles were resuspended in 2 mL of H_2O.

Characterisation of HNPs

Powder X-ray diffraction (PXRD) was used to determine the nature of the magnetic iron oxide synthesised. PXRD patterns were obtained from a Bruker D8 Advance X-ray diffractometer using a flat disc sample holder from 10° to 70° (2θ), using Cu Kα radiation, a 0.04° (2θ) step size and a data collection time of 7 s per step. Inductively coupled plasma-optical emission spectroscopy (ICP-OES) was used to determine the metal composition of the particles. An acid digestion was carried out using HNO$_3$ (1:5 sample:acid). The samples were diluted with deionised water prior to analysis. A calibration was run using iron and gold standard solutions 0.5–10 μg mL^{-1} ($R = 0.9999$). Polymer concentration was estimated using elemental analysis and via ninhydrin amine quantification assay and also using thermogravimetric analysis (TGA). The TGA was carried out on a TA SDT Q600 (TA Instruments) with sequences of 20 °C min^{-1} ramp to 90 °C, isothermal for 10 min and 20 °C min^{-1} ramp to 600 °C. Hydrodynamic diameters and polydispersity index were measured using a photon correlation spectrometer (PCS) (Zetasizer Nano-ZS, Malvern Instruments, UK). The measurements were conducted at 25 °C in triplicate and an average value was determined. The zeta potential of the nanoparticle solutions was analysed to determine surface charge using the same instrument. Transmission electron microscopy (TEM) was carried out in order to visualise the particle morphology. Samples diluted in deionised water were dropped onto formvar-coated copper grids (2 μL) and allowed to dry at room temperature. The grids were directly imaged using a JEOL JEM-1230 microscope using analysis software (JEOL, Japan). Polymer-coated HNP solutions (5 mL) were freeze-dried for Fourier transform infrared (FTIR) spectroscopy. The dry powder was measured using a diamond tipped attenuated total reflectance attachment (Nicolette IS50, Thermo-Fisher UK). The samples were scanned 64 times and the average spectra recorded. Peak absorbance of aqueous samples was measured using a Varian UV–Vis Cory 50 Bio spectrometer (Varian, UK). Samples were analysed in quartz cuvettes, absorbance scans were carried out between 200 and 800 nm.

Magnetic characterisation

Magnetisation measurements

Magnetic characterisation of the samples was carried out in a Quantum Design MPMS-XL SQUID magnetometer. Zero-field-cooled warming (ZFCW) and

field-cooled cooling (FCC) curves were measured between 10 and 280 K, in an applied magnetic field $H = 8$ kA m^{-1}. For the ZFCW curves, the samples were first cooled from room temperature in zero applied field to the base temperature (5 K). Then a field was applied and the temperature dependence of the magnetisation was measured. The FC curves were taken by cooling the sample in the same field. Magnetisation versus applied field hysteresis loops were collected at 10 and 250 K in applied fields of up to 4 MA m^{-1}.

Magnetic resonance relaxivity measurements

Particles were immobilised in 2 % agar (0.05–50 μg mL^{-1}) inside 7 mL bijou vials (Starlabs, UK). Relaxivity measurements were carried out at 19 °C in a 1.5 T MRI scanner (Signa HDx, GE, USA) using GE's receive-only HD 8-channel head coil. T_1 and T_2 relaxation times were measured using the Inversion Recovery Spin-Echo (IRSE) and Spin-Echo (SE) sequences, respectively, on a single coronal slice intersecting the gel with nanoparticles. The imaging parameters for the IRSE were as follows: repetition time (TR) = 15 s; echo time (TE) = 9 ms; acquisition matrix = 128 × 128; field of view (FOV) = 20 cm; band width (BW) = 15.63 kHz; number of excitations (NEX) = 1; slice thickness = 8 mm; inversion time (TI) of 100, 200, 400, 600, 800,1000, 1200, 1400 1600, 1800, 2000 and 2200 ms. The SE parameters were as above with TE of 10, 20, 30, 50, 70, 100, 120, 150, 200, 250, 300, 350, 400, 450, 500, 550, 600, 650, 700, 750, 800, 850 and 900 ms. Regions of interest (ROI) were selected in each vial over the image set and T_i ($i = 1$ and 2) values were calculated from the three-parameter nonlinear least squares fit of the mean signal intensities versus time (TI and TE, respectively) data. The associated relaxivities (r_i in mM^{-1} s^{-1}) were obtained from the gradient of the linear least squares fit of the relaxation rates ($R_i = 1/T_i$) versus concentration of Fe (mM).

Laser irradiation of HNPs in agar gel

HNPs were dispersed in 2 % agar at 10 μg mL^{-1}. The gels were formed in shallow, 35 mm diameter plastic petri dishes (Greiner, UK). The immobilised samples were exposed to laser irradiation at 532 nm using a Q-switched Nd:YAG laser (10 ns pulses, 10 pulses s^{-1}).

The beam was collimated in a 7 mm diameter and passed through the gel centre. The temperature change was monitored using 0.076 mm diameter PFA-coated T-type thermocouples (Omega, UK). One thermocouple was positioned at the centre of the gel with a second placed at the edge of the gel as a control. All measurements were carried out at room temperature, 25 °C. Sample irradiation was carried out over 1 min. The temperature change in a control sample (2 % agar) was measured in the absence of nanoparticles.

Results and discussion

Characterisation of iron oxide cores

Iron oxide cores were synthesised in three different diameters—small (S), medium (M) and large (L). PXRD analysis determined that the particles matched the reference patterns for magnetite (Fe_3O_4) (Supplementary Material, Fig. 1). The particle diameter was characterised using TEM (Fig. 1) and photon correlation spectroscopy (PCS) (Table 1). Here there was a large size discrepancy between the two methods of measurement. This was largely due to the aggregation of the uncoated iron oxide cores upon suspension in liquid to form large clusters of 2250, 2159 and 2171 nm (Fe_3O_{4S}, Fe_3O_{4M} and Fe_3O_{4L}, respectively) due to their inherent magnetism. The TEM allowed direct visualisation of the particles and here a more accurate particle diameter could be obtained [50(1.1), 120(2.1) and 200(2.2) nm, respectively ($n = 20 \pm$ SD)]. Interestingly, at the largest diameter the particle morphology changed from a spherical to a hexagonal shape. This phenomenon is due to the crystal habit, whereby growth occurs on preferred interfaces of the nanoparticle due to the sulphate presence in the reaction (Andrés Vergés et al. 2008). Zeta potential measurements showed negative surface charge on the particles (Table 1), this too can be attributed to the sulphate association due to the reaction precursors (Andrés Vergés et al. 2008). Iron content was analysed using ICP-OES (Table 1).

Effect of polymer intermediate on physical properties of HNPs

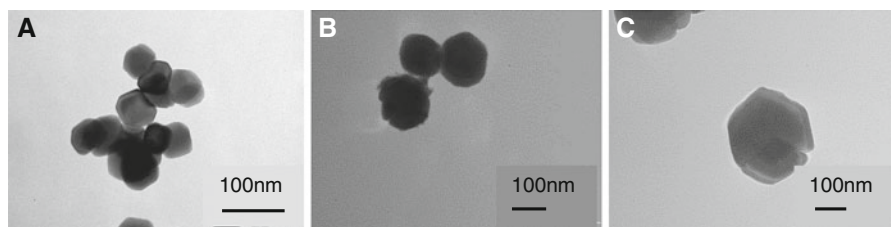Three cationic polymers were added to electrostatically coat the Fe_3O_{4S} surface. FTIR indicated the

Fig. 1 TEM images of iron oxide core showing diameters of **a** Fe_3O_{4S}, **b** Fe_3O_{4M} and **c** Fe_3O_{4L}

Table 1 Hydrodynamic diameter and surface charge of iron oxide nanoparticles and hybrids measured using PCS and zeta potential measurements ($n = 3$)

Particle	Metal content analysis ($\mu g\ mL^{-1}$)		Size, nm ($\pm$SD)	PDI ($\pm$SD)	Zeta potential, mV ($\pm$SD)
	Fe	Au			
Fe_3O_{4S}	7000	–	2250 (125)	0.540 (0.125)	−16.5 (1)
Fe_3O_{4M}	5215	–	2159 (154)	0.675 (0.012)	−17.2 (1)
Fe_3O_{4L}	6542	–	2171 (321)	0.823 (0.054)	−19.4 (1)
Fe_3O_{4S}–PEI	1920	–	270 (11)	0.125 (0.004)	+47.4 (3)
Fe_3O_{4M}–PEI	2651	–	208 (7)	0.321 (0.012)	+50.2 (3)
Fe_3O_{4L}–PEI	1307	–	328 (9)	0.147 (0.001)	+55.2 (2)
Fe_3O_{4M}–PAA	1994	–	217 (11)	0.297 (0.015)	+51.2 (2)
Fe_3O_{4M}–PLL	1897	–	1542 (121)	0.875 (0.125)	+10.2 (1)
Fe_3O_{4S}–PEI–Au_{SEED}	1025	45	190 (9)	0.254 (0.001)	+27.5 (1)
Fe_3O_{4M}–PEI–Au_{SEED}	1002	59	201 (12)	0.372 (0.004)	+32.4 (2)
Fe_3O_{4L}–PEI–Au_{SEED}	1212	29	255 (31)	0.154 (0.032)	+35.5 (0)
Fe_3O_{4M}–PAA–Au_{SEED}	1045	95	187 (17)	0.111 (0.024)	+31.2 (2)
Fe_3O_{4S}–PEI–Au_{COAT}	990	370	115 (5)	0.258 (0.011)	+10.5 (0)
Fe_3O_{4S}–PEI–$Au_{COAT-THICK1}$	982	1411	190 (19)	0.152 (0.012)	+5.3 (0)
Fe_3O_{4S}–PEI–$Au_{COAT-THICK2}$	1025	2510	250 (22)	0.112 (0.010)	+2.4 (0)
Fe_3O_{4M}–PEI–Au_{COAT}	852	218	124 (12)	0.114 (0.002)	+12.2 (1)
Fe_3O_{4L}–PEI–Au_{COAT}	970	490	162 (13)	0.123 (0.001)	+15.6 (0)
Fe_3O_{4S}–PAA–Au_{COAT}	831	277	122 (21)	0.109 (0.090)	+12.5 (1)

successful attachment of both the PEI and PAA (Supplementary Material, Fig. 2). Here, –NH peaks were present at 3300, 1700 and 1600 cm^{-1} along with a C–N peak at 1000 cm^{-1} which are the characteristic vibrational energies of the bonds present in the polymer backbone. These peaks were not observed on analysis of the uncoated Fe_3O_4 or Fe_3O_{4S}–PLL (data not shown). Elemental analysis data (Supplementary Material, Table 1) confirmed the attachment of PEI and PAA onto the nanoparticle surface due to the presence of C, H and N abundance. These elements are attributed to the atoms on the polymer backbone which were not observed when the uncoated core were analysed. Ninhydrin assay allowed quantification of

the primary amines within the polymer structures. Here, we calculated the polymer concentration to be 89 and 106 $\mu g\ mL^{-1}$ per 1 mg Fe^{3+} for PEI and PAA, respectively. Elemental analysis of the PLL-coated particles showed that the polymer was less abundant compared with the PEI and PAA, ninhydrin quantification confirmed this finding with only 36 $\mu g\ mL^{-1}$ polymer per 1 mg Fe^{3+}. Both the PEI and PAA are long chain polymers of molecular weight (MW) 750,000 and 120–200,000 (PEI and PAA, respectively). The PLL used in this study hand an estimated MW 30–60,000. It is proposed that the mechanisms of polymer coating is as follows. The high MW PEI and PEI wrap around the nanoparticle surface forming a

dense mesh, whereas the lower MW PLL possesses reduced ability to wrap around the negatively charged iron oxide core resulting in an incomplete coating (Fig. 2). This idea is supported by the zeta potential measurements ($+47.4$, $+51.2$ and $+10.2$ mV for PEI-, PAA- and PLL-coated Fe_3O_{4S}, respectively, Table 1) and TGA (Supplementary material, Table 1). Due to the relatively low surface charge of the PLL-coated particles these were not investigated any further in this study. Addition of the PEI and PAA onto the iron oxide nanoparticle resulted in a diameter increase of 10(1) nm in both cases.

Figure 3 shows the magnetisation versus applied field hysteresis loop collected at 250 K for the samples. The magnetic coercivity (Table 2) and saturation magnetisation values at $T = 250$ K are indicative of highly crystalline Fe_3O_4 nanoparticles which are magnetically ordered at room temperature (Riggio et al. 2012). The magnetic coercivity (Hc) of the PEI-coated core (9.70 kA m^{-1}) is similar to the value for the PAA (10.50 kA m^{-1}) and PLL-coated particles (10.35 kA m^{-1}). This can be attributed to the particles possessing identical magnetic cores to the uncoated particle (10.95 kA m^{-1}). Here, coating with each of the polymers did not result in any notable change in Hc values (Table 2). The zero-field-cooled/field-cooled curves (Supplementary Material, Fig. 3) showed features typical of ferromagnetic nanoparticles (Riggio et al. 2012). The absence of a maximum in this data shows that the ordering temperature is above room temperature (Andrés Vergés et al. 2008).
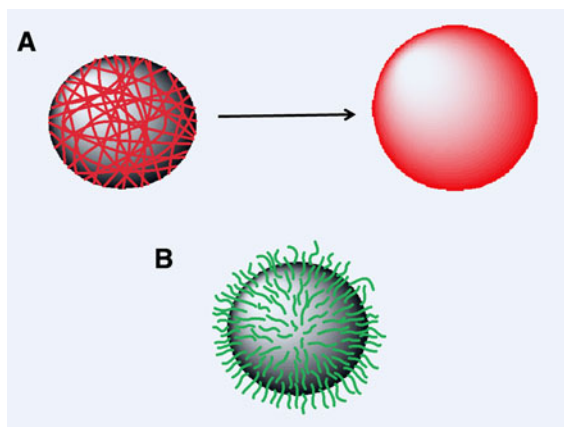

Fig. 2 Proposed mechanism of polymer coating of Fe_3O_4 core through an electrostatic interaction with *a* PEI and PAA and *b* PLL

When compared to Feridex® (1.2 kA m^{-1}) the polymer-coated nanoparticles possess much greater Hc values. This is due to the larger-sized nanoparticles possessing ferromagnetic properties rather than the superparamagnetic properties exhibited by Feridex®.

Table 2 shows the influence of polymer coating on T_2 values across the coating steps. MRI agents with higher T_2 relaxivity values are more desirable as they produce higher contrast images. The T_2 value of the uncoated Fe_3O_{4S} was 127.6 mM^{-1} s^{-1}. Upon polymer coating no major change in relaxivity was observed with the PAA (121 mM^{-1} s^{-1}) or PLL (149 mM^{-1} s^{-1}). However, coating with PEI increased the relaxivity twofold up to 266.2 mM^{-1} s^{-1}. This large increase in T_2 relaxivity suggests that the presence of the PEI increases particle contrast ability compared with the 'naked' core resulting in a more effective T_2-MRI contrast agent.

Gold seeding onto polymer-coated iron oxide cores was achieved by electrostatic interaction between the negatively charged gold seeds (2 nm) and the positively charged nanoparticles, followed by reduction of HAuCl$_4$ to form a complete coat. Figure 4a shows a schematic diagram of the four stages of HNP coating from uncoated (Fig. 4a1) to fully gold coated (Fig. 4a4). The TEM images for the coating of Fe_3O_{4S}–PEI are shown in Fig. 4B1–4. Here the characteristic 'bobbly' appearance of the gold seed attached can be clearly observed (Fig. 4b3) followed by the smooth spherical appearance of the Fe_3O_{4S}–PEI–Au$_{COAT}$ (Fig. 4b4). Interestingly, once complete Fe_3O_{4S}–PAA gold coating had been achieved, a star-shaped morphology was observed (Fig. 4c1). The reason for this non-spherical morphology is not entirely clear. Perhaps the PAA promotes the growth of the gold in the iterative additions in a different manner to the PEI. The TEM images show that both the fully coated particles (containing the 50 nm diameter iron oxide core + 10 nm polymer) are 70 nm in diameter resulting in a gold coat of 5 nm thick. ICP-OES was used to determine metal content of the nanoparticles (Table 1). The data agrees with the TEM images, whereby a coating of similar thickness was obtained for both particles with 3:1 Fe:Au metal content ratio. The zeta potential measurements (Table 1) showed a reduction in the degree of positive surface charge. This is due to the electronegative gold shielding the polycationic polymer and reducing the overall charge. UV absorption spectroscopy measurements (Fig. 5) showed the coated

Fig. 3 Magnetisation data of metallic nanoparticles. **a** Magnetisation versus applied field M(H) at 250 K Fe_3O_{4S}, Fe_3O_{4S}–PEI, Fe_3O_{4S}–PAA, Fe_3O_{4S}–PLL and Feridex® between **a1** −20 and +20 kA m^{-1} and **a2** −4 and +4 MA m^{-1}. **b1** Fe_3O_{4s}–PEI–Au$_{COAT}$, Fe_3O_{4S}–PAA–Au$_{COAT}$, Fe_3O_{4s}–PEI–Au$_{COAT-THICK1}$, Fe_3O_{4s}–PEI–Au$_{COAT-THICK2}$ and **b2** Fe_3O_{4s}–PEI–Au$_{COAT}$, Fe_3O_{4M}–PEI–Au$_{COAT}$ and Fe_3O_{4L}–PEI–Au$_{COAT}$ between −20 and 20 kA m^{-1}
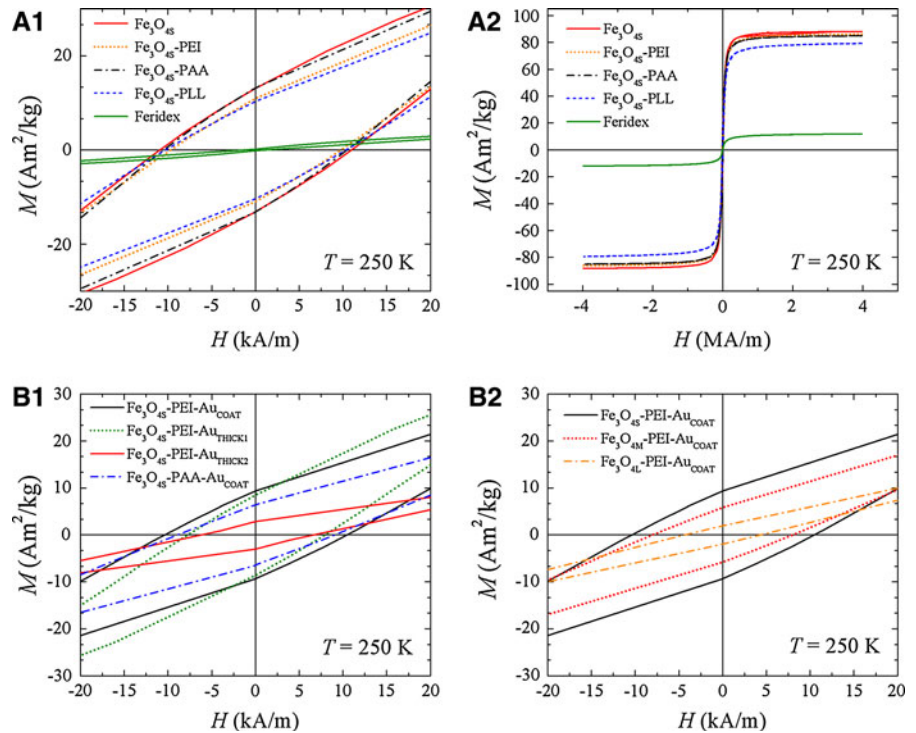
Table 2 Magnetic coercivity and T_2 relaxivity of nanoparticles determined from the SQUID magnetometry analysis and MRI (1.5 tesla) data, respectively

Particle	Hc, kA m^{-1} (±SD)	T_2 relaxivity, mM^{-1} s^{-1} (±SD)
Fe_3O_{4S}	10.95 (5)	127.6 (11)
Fe_3O_{4S}–PEI	9.70 (5)	260.2 (1)
Fe_3O_{4S}–PAA	10.5 (5)	121.3 (2)
Fe_3O_{4S}–PLL	10.35 (5)	147.8 (17)
Fe_3O_{4S}–PEI–Au$_{COAT}$	10.35 (5)	175.3 (1)
Fe_3O_{4S}–PEI–Au$_{COAT-THICK1}$	7.73 (5)	350.8 (5)
Fe_3O_{4S}–PEI–Au$_{COAT-THICK2}$	6.45 (5)	38.7 (3)
Fe_3O_{4S}–PAA–Au$_{COAT}$	8.76 (5)	385.5 (3)
Fe_3O_{4M}–PEI–Au$_{COAT}$	8.04 (5)	246.7 (3)
Fe_3O_{4L}–PEI–Au$_{COAT}$	4.42 (5)	264.5 (6)
Feridex®	1.20 (5)	240.4 (2)

particles to possess a broad absorption band with maximum around 690 nm. This wavelength is approaching the near infrared (NIR) 'biological window' where high tissue transmittance of light is observed. It is hypothesised that by further surface functionalisation the peak absorbance should further red-shift into this window above 750 nm. The spectra looked similar for both the PEI and PAA nanoparticles (the difference in absorbance strength can be attributed to concentration differences in sample measurement). No peak absorbance was observed with the uncoated or polymer-coated Fe_3O_4 (data not shown).

Figure 3b1 shows the M(H) curves for Fe_3O_{4S}–PEI–Au$_{COAT}$ and Fe_3O_{4S}–PAA–Au$_{COAT}$. The values extracted from the curves showed that there is a very slight increase in coercivity for the Fe_3O_{4S}–PEI–Au$_{COAT}$ sample after gold coating (10.35 kA m^{-1}) whilst the Fe_3O_{4S}–PAA–Au$_{COAT}$ exhibits a decrease in Hc (8.76 kA m^{-1}) (Table 2). Overall, the Hc values of the gold-coated HNPs were similar with no notable difference with varied polymer intermediate. The ZFCW/FCC curves for Fe_3O_{4S}–PEI–Au$_{COAT}$ and Fe_3O_{4S}–PAA–Au$_{COAT}$, respectively, can be viewed in the supplementary data (Fig. 3b).

After gold coating, the T_2 relaxivity of the nanoparticle was increased compared with the polymer-coated particles and uncoated core (Table 2). Interestingly, the PAA nano-star showed a threefold increase in T_2 relaxivity (386 mM^{-1} s^{-1}) compared

with the uncoated core. It is proposed that the nano-star configuration results in an increased particle surface area which may contribute to increased relaxivity. This value is 1.6 times higher than Feridex® (240 mM^{-1} s^{-1}) measured on the same system under identical conditions (these findings are consistent with the conclusions drawn from the analysis of the magnetometry data).

The HNPs were suspended in agar, irradiated with laser light and the change in temperature recorded. Here, we used a nanosecond (Q-switched) pulsed laser at 532 nm. Although this laser is not in the NIR region, the range of wavelengths absorbed by the particles is very broad and as so heating effects are still be expected. A laser of around 750 nm would have better suited to this application and resulted in more biologically relevant results, however, this laser study can still be used to show the influence of the HNP structure and morphology on the ability of the particles to act as nano-heaters. The nanoparticles (10 µg mL^{-1}) were irradiated for up to 1 min and compared with an agar
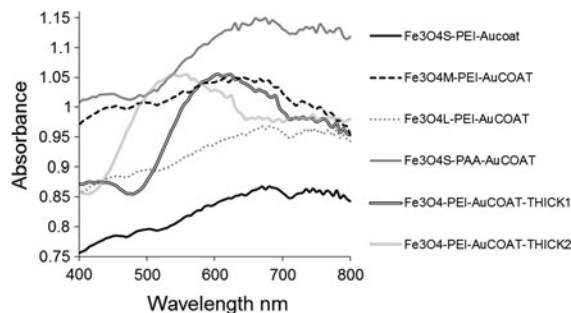
Fig. 5 UV absorption of gold-coated Fe$_3$O$_4$ nano-hybrids. Samples analysed in deionised water, at room temperature and scanned between 400 and 800 nm. All measurements taken using a 1-cm path length quartz cuvette

control. The results showed that after 60 s both the Fe$_3$O$_{4S}$–PEI–Au$_{COAT}$ and Fe$_3$O$_{4S}$–PAA–Au$_{COAT}$ had experienced at 7 °C temperature increase. Looking at the data (Fig. 6), it is evident that the heating profile looks different for both cases. For the PEI intermediate nanoparticle, a smooth heating curve is observed
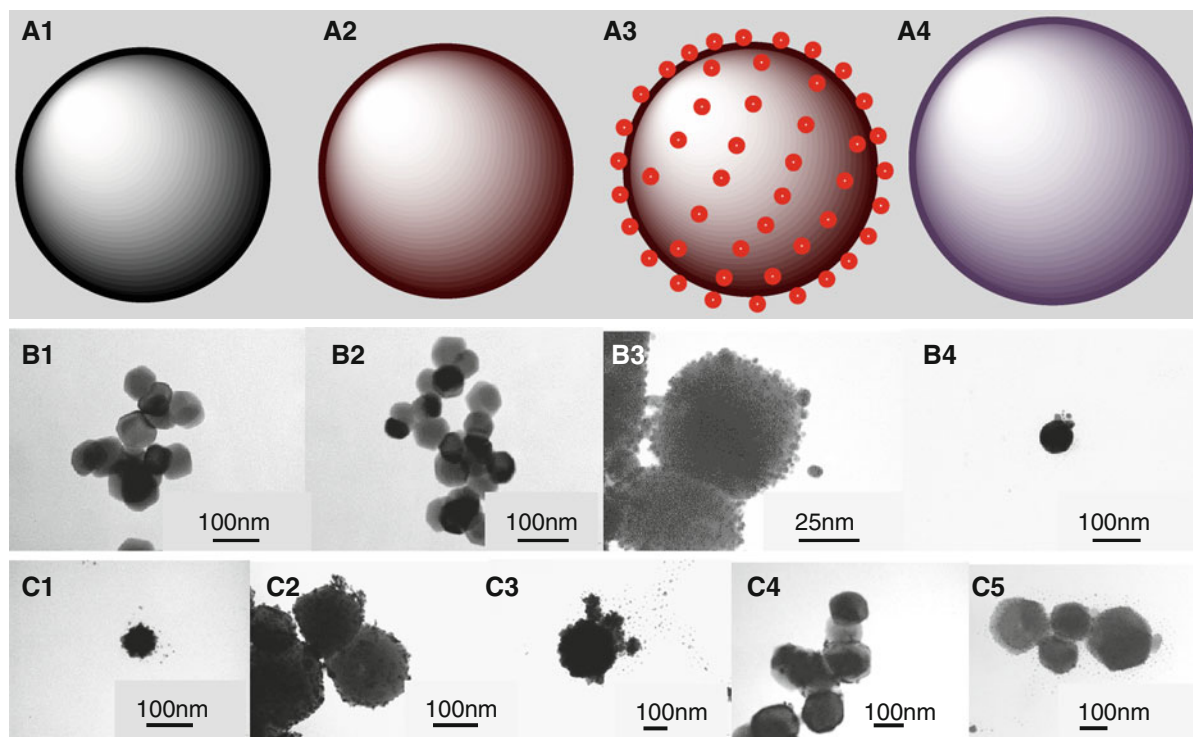
Fig. 4 Coating steps of Fe$_3$O$_4$–Au HNPs. **a** Schematic diagram and **b** TEM of **b1** Fe$_3$O$_4$, **b2** Fe$_3$O$_4$–PEI, **b3** Fe$_3$O$_4$–PEI–Au$_{SEED}$ and **b4** Fe$_3$O$_4$–PEI–Au$_{COAT}$ (images using Fe$_3$O$_{4S}$ core). **c** Fully coated particles with varied parameters **c1** Fe$_3$O$_{4S}$–PAA–Au$_{COAT}$, **c2** Fe$_3$O$_{4S}$–PEI–Au$_{COAT-THICK1}$, **c3** Fe$_3$O$_{4S}$–PEI–Au$_{COAT-THICK2}$, **c4** Fe$_3$O$_{4M}$–PEI–Au$_{COAT}$ and **c5** Fe$_3$O$_{4L}$–PEI–Au$_{COAT}$

whereas, in the case of the PAA intermediate, the curve contains oscillations. This could be due to the uneven surface of the star-shaped particles resulting in an uneven heating pattern due to an unusual absorption and scattering phenomenon. Here, the Fe_3O_{4S}–PAA–Au_{COAT} nanoparticles heated up more rapidly than the Fe_3O_{4S}–PEI–Au_{COAT} particles; however, the heating appeared to be reaching a plateau at increased irradiation times.

Effect of gold coating thickness on physical properties of HNPs

Previous reports have suggested that gold nano-shells were more efficient as nano-heaters than gold nano-particles (Yavuz et al. 2009; Prodan et al. 2003). This is due to the increased surface area of the nano-shell (taking into account the internal and external surfaces) (Wang et al. 2007). We have already shown the ability of the PAA nano-stars to possess optimal MRI capabilities and unique nano-heating profiles when compared with PEI nano-spheres. We earlier postulated that this could be due to increased surface area of the nano-stars coupled with the PAA promoting optimal relaxivity. However, little is known about the effect on all the physical attributes of nano-spheres at differing gold shell thickness. Here, we coated iron oxide cores of identical diameter and polymer coating (Fe_3O_{4S}–PEI) with differing thickness of gold. The coating thickness was varied by using increased numbers of iterative addition steps during the gold coating process. Three coating thicknesses were
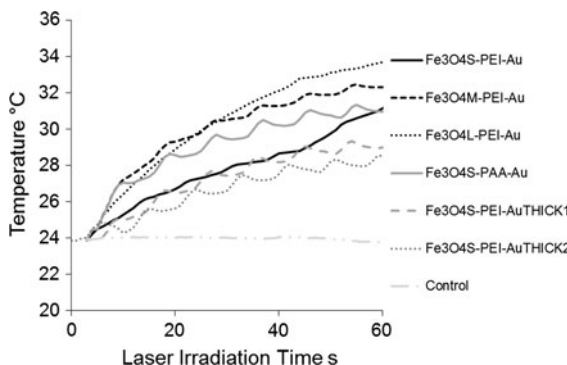

Fig. 6 Temperature change in HNPs exposed to laser irradiation using a Q-switch Nd:Yag laser at 10 pulses s^{-1}. Samples consisted of 10 µg mL^{-1} HNPs suspended in 2 % agar. All samples equilibrated to room temperature before beginning. Control sample consisted of 2 % agar with no nanoparticles

achieved, 5 nm (Fig. 4b4), 50 nm (Fig. 4c2) and 100 nm (Fig. 4c3) forming particles of diameter 70, 160 and 260 nm, respectively. Interestingly, the particle with the 50 nm gold coat appeared to possess a 'bobbly' surface much like the image acquired for the seeded particles showing the initiation of nano-star formation whereby, the gold was preferentially growing at anchor points (Kumar 2008; Yuan et al. 2012). The large star-shaped particles were observed upon further gold coating up to 100 nm thickness. ICP analysis (Table 1) showed the metal content ratio of Fe:Au to decrease from 3:1 to 0.7:1 to 0.4:1 upon addition of the thicker coat. Zeta potential measurements showed a reduction in the surface charge in the Fe_3O_4–PEI–$Au_{COAT-THICK1}$ (+10.5 mV) and Fe_3O_4–PEI–$Au_{COAT-THICK2}$ (+2.4 mV) compared with the Fe_3O_4–PEI–Au_{COAT} (+5.3 mV) (Table 1). Previous reports have suggested that gold shells with reduced thickness are shifted further towards the NIR region resulting in more efficient heating (Kumar 2008). Our UV data supported this trend with the absorbance maxima shifting back towards 530 nm with the 100 nm coating (Fig. 5). Other gold nanoparticle studies have reported an increased red-shifting in the UV absorbance values with increased particle diameter (Link and El-Sayed 1999). Here, we observed a large decrease despite the overall particle diameter increasing.

Hc values extracted from the M(H) hysteresis loops (Fig. 3b1) showed that increasing the gold nano-shell thickness resulted in a decrease in Hc from 10.35 kA m^{-1} with a 5 nm coat thickness to 7.73 kA m^{-1} (50 nm coat) and 6.45 kA m^{-1} with the 100-nm thick coat (Table 2). Here, the increased shell thickness results in an increased core shielding leading to a reduction in magnetic effect. The T_2 relaxivity data was overall in agreement with this finding (Table 2). According to our data, the relaxivity of the nanoparticles is notably increased upon addition of a 50-nm thicker gold coating. The relaxivity of the Fe_3O_{4S}–PEI–$Au_{COAT-THICK1}$ was 1.6 times greater than Feridex®. This data is in disagreement with other reports, where increased thickness of any coat leads to a shielding effect on the iron oxide core, reducing its T_2 contrast ability (LaConte et al. 2007). The TEM for the Fe_3O_{4S}–PEI–$Au_{COAT-THICK1}$ particles suggested initiation of nano-star formation had occurred. Comparison of the TEM and MRI data with Fe_3O_{4S}–PAA–Au_{COAT} showed similar phenomenon whereby particles in the star-shaped morphology appeared to result in larger relativity values. This difference could be due to the

rigid coating used here compared with the flexible PEG polymer used in the previous study. However, upon increasing the gold coating thickness to 100 nm the relaxivity drastically decreased to 38.7 mM^{-1} s^{-1} in line with previous studies (LaConte et al. 2007).

The addition of a thicker layer of gold coating onto the nanoparticles appeared to reduce their ability to act as nano-heaters (Fig. 6) after laser irradiation. Here, a 4 °C reduction in temperature at 60 s irradiation was observed for Fe$_3$O$_{4S}$–PEI–Au$_{COAT-THICK1}$ compared to the Fe$_3$O$_{4S}$–PEI–Au$_{COAT}$ and this trend followed upon further coating. Similar to the nano-star observed using the PAA intermediate, the 50 and 100 nm gold-coated nanoparticles appeared to have an oscillating heating pattern. This result was in agreement with the TEM imaging whereby, an uneven surface was observed which may result in an unusual scattering/ absorption pattern.

Effect of core diameter on physical properties of HNPs

Increasing the core diameter of magnetic the particles from the nano to the micrometre scale will change the cores from superparamagnetic particles to multi-domain ferromagnetic particles. Superparamagnetic nanoparticles only possess a single magnetic domain in which all the magnetic spins are aligned; in the presence of an external magnetic field these domains may be aligned with the thermal motion of the particles controlling the bulk magnetic properties (Gupta and Gupta 2005; Suh et al. 2009; Wang et al. 2001; Neuberger et al. 2005). Ferromagnetic particles are larger and can have more than one magnetic domain resulting in a stronger magnetic effect. We have produced gold-coated ferromagnetic particles in three diameters of the order 70 nm (Fig. 4b4), 140 nm (Fig. 4c4) and 220 nm (Fig. 4c5). Zeta potential measurement of the uncoated core decreased slightly from −16.5 to −17.2 to −19.4 mV (respectively) due to the increased surface area resulting in an increased net negative potential.

Gold was applied resulting in a complete coating of 10 nm thickness. UV spectroscopy showed no major deviation in maxima absorbance values through the size range (Fig. 5). This is interesting considering the properties of gold nanoparticles where absorbance maxima increases with particle diameter. The spectra did, however, possess two peaks at 690 and 750 nm for

all three samples with no preference to 750 nm with increased particle diameter. Figure 3b2 shows M(H) hysteresis loops for the Fe$_3$O$_{4S}$–PEI–Au$_{COAT}$, Fe$_3$O$_{4M}$–PEI–Au$_{COAT}$ and Fe$_3$O$_{4L}$–PEI–Au$_{COAT}$ particles. This data suggest that nanoparticles with these diameters (50, 120 and 200 nm) form soft ferromagnetic systems (Table 2). The ZFCW/FCC curves for the three samples (Supplementary data, Fig. 3C) showed no obvious differences. This is expected as the similar synthesis procedure is likely to produce magnetic iron oxide produced with comparable properties. The M(H) curves (Supplementary data, Fig. 3D) suggest that as the particle diameter is increased the saturation magnetism decreases. However, further analysis needs to be carried out to confirm this.

The effect on T_2 relaxivity on increasing core diameter can be seen in Fig. 7. As expected, increasing core diameter resulted in a greater T_2 relaxation which suggests that these nanoparticles would act as a very effective T_2 contrast agents. The relaxivity of the Fe$_3$O$_{4M}$–PEI–Au$_{COAT}$ and Fe$_3$O$_{4L}$–PEI–Au$_{COAT}$ were similar (247 and 265 mM^{-1} s^{-1}, respectively) probably due to the relative closeness in nanoparticle diameter compared with the smaller particle (175 mM^{-1} s^{-1}) (Table 2). Laser irradiation showed that the optimal heating was observed in particles as follows Fe$_3$O$_{4S}$–PEI–Au$_{COAT}$ < Fe$_3$O$_{4M}$–PEI–Au$_{COAT}$ < Fe$_3$O$_{4L}$–PEI–Au$_{COAT}$. The rationale behind the larger diameter
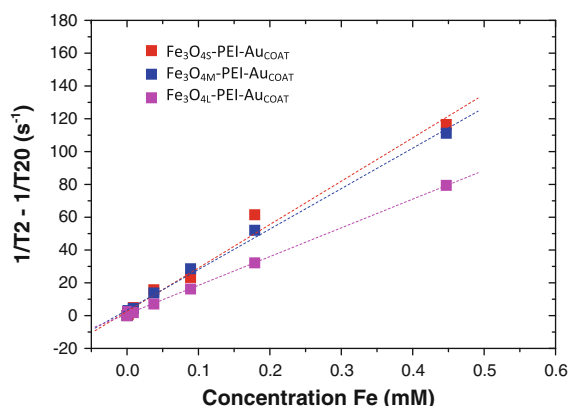
Fig. 7 Relaxation rates as a function of concentration of Fe in HNPs. The *dotted line* represents the linear fit to the experimental data. The transverse relaxivities (r_2, mM^{-1} s^{-1}) were calculated as the gradient of the *straight lines* fitted to the experimental data

producing larger thermal energy can be attributed to the larger surface area of the gold nano-shell absorbing greater photonic energy. Oddly, the 120 nm particles showed a heating profile similar to the PAA nano-star conformation particles with heating oscillations apparent (Fig. 6). This suggests that the gold coating is also starting to form the nano-star morphology; however, this is not supported by TEM imaging (Fig. 4c4) where minute spindles or anchor points are not evident. Further investigation into this phenomenon is on-going.

Conclusions

In order for HNPs to be of optimal relevance in biomedicine their unique characteristics need to be fully understood and exploited. Understanding the importance of the structural composition and morphology are key to developing efficient systems. In general, gold coating of magnetic iron oxide particles using a polymer intermediate between the core and the shell resulted in increased ability of the particles to act as negative contrast agents for MR imaging. The data also showed that the polymer intermediate and shell thickness can promote gold shell formation in differing morphologies such as spherical and star like structures. Previously nano-stars have been reported to lead to increased heating effects upon laser irradiation compared to nano-spheres. Although the findings from this study found no difference, they do show that nano-stars exhibit unique heating profiles, and that they also possess larger T_2 values when compared to spherical structures. On-going investigations are being carried out in order to fully understand this phenomenon. The effect of magnetic iron oxide core diameter on the magnetisation of the hybrid molecule was also tested.

The great beauty of nano-medicine is the ability to passively target tissues due to the effects of enhanced permeability and retention. These effects are witnessed in rapidly proliferating cancerous tissues which do not have time to fully form. With this in mind, we suggest that for image guided tumour ablation or thermo-responsive anticancer drug delivery, hybrid molecules with a smaller particle diameter would be more appropriate as this can result in a greater accumulation of particles and a more pronounced heating effect. In this study, we have reported temperature increases up to 10 °C at 10 µg mL^{-1}

(a realistic administration concentration) over only 60 s. This degree of temperature increase over short exposure periods is sufficient to induce cellular hyperthermia or thermal drug delivery. The requirements necessary to mitigate any toxicological effect and inflammatory response must be considered before biological applications are possible. Therefore, it is of utmost importance to carefully construct nanoparticles which will exhibit the desired effects such as magnetism or photon absorption at relevant concentrations. In order to facilitate this, further work is being carried out in our laboratory to investigate the stability and biological relevance of these HNPs for medical application.

References

Andrés Vergés M, Costo R, Roca AG, Marco JP, Goya GF, Serna CJ, Morales MP (2008) Uniform and water stable magnetite nanoparticles with diameters around the monodomain–multidomain limit. J Phys D Appl Phys 41: 134003

Ansari SA, Hussain Q (2011) Immobilization of kluyveromyces lactis β galactosidase on concanavalin A layered aluminium oxide nanoparticles—its future aspects in biosensor applications. J Mol Catal B Enzymatic 70:119–126

Ansari SA, Hussain Q, Qayyum S, Azam A (2011) Designing and surface modification of zinc oxide nanoparticles for biomedical applications. Food Chem Toxicol 49:2107–2115

Bhattacharya R, Mukherjee P (2008) Biological properties of "naked" metal nanoparticles. Adv Drug Deliv Rev 60: 1289–1306

Bystrejewski M, Cudzilo S, Huczko A, Lange H, Soucy G, Cota-Sanchez G, Kaszuwara W (2007) Carbon encapsulated

magnetic nanoparticles for biomedical applications @ thermal stability studies. Biomol Eng 24:555–558

Chen S, Hoskins C, Wang L, MacDonald WP, André PA (2012) A water-soluble temperature nanoprobe based on a multi-modal magnetic-luminescent nanocolloid. Chem Commun 48:2501–2503

Fadeel B, Garcia-Bennett AE (2010) Better safe than sorry: understanding the toxicological properties of inorganic nanoparticles manufactured for biomedical applications. Adv Drug Deliv Rev 62:362–374

Fraga CG, Arias RF, Llesuy SF, Koch OR, Boveris A (1987) Effect of vitamin E- and selenium-deficiency on rat liver chemiluminescence. Biochem J 242:383–386

Goon IY, Lai LMH, Lim M, Munroe P, Gooding JJ, Amal R (2009) Fabrication of gold-shell-protected magnetite nanoparticles: systematic control using polyethyleneimine. Chem Mater 21:673–681

Guerrero-Martínez A, Barbosa S, Pastoriza-Santos I, Liz-Marzán LM (2011) Nanostars shine bright for you, colloidal synthesis, properties and applications of branched metallic nanoparticles. Curr Opin Colloid Interface 16:118–127

Gupta AK, Gupta M (2005) Synthesis and surface engineering of iron oxide nanoparticles for biomedical applications. Biomaterials 26:3995–4021

Hoskins C, Wang L, Cuschieri A (2012a) The cytotoxicity of polycationic nanoparticles: common endpoint assays and alternative approaches for improved understanding of cellular response mechanism. J Nanobiotechnol 10:15

Hoskins C, Min Y, Gueorguieva M, McDougall C, Volovick A, Prentice P, Wang Z, Melzer A, Cuschieri A, Wang L (2012b) Hybrid gold–iron oxide nanoparticles as a multi-functional platform for biomedical application. J Nanobiotechnol 10:27

Jain PK, El-Sayed IH, El-Sayed MA (2007) Au nanoparticles target cancer. Nano Today 2:18–29

Ji X, Shao R, Elliott AM, Stafford J, Esparza-Coss E, Bankson JA, Liang G, Luo Z-P, Park K, Markert J-T, Li C (2007) Bifunctional gold nanoshells with a superparamagnetic iron oxide–silica core suitable for both MR Imaging and photothermal therapy. J Phys Chem C 111:6245–6251

Kumar CSSR (2008) Metallic nanomaterials. Wiley–VCH Verlag GmbH, Weinheim

LaConte LE, Nitin N, Zurkiya O, Caruntu D, O'Connor CJ, Hu X, Bao G (2007) Coating thickness of magnetic iron oxide nanoparticles affects R2 relaxivity. J Magn Reson Imaging 26:1634–1641

Link S, El-Sayed MA (1999) Size and temperature dependence of the plasmon absorption of colloidal gold nanoparticles. J Phys Chem B 103:4212–4217

Minotti G, Aust SD (1987) The requirement for iron(III) in the initiation of lipid peroxidation by iron(II) and hydrogen peroxide. J Bio Chem 262:1098–1104

Neuberger T, Schöpf B, Hofmann H, Hofmann M, von Rechenberg B (2005) Superparamagnetic nanoparticles for biomedical applications: possibilities and limitations of a new drug delivery system. J Magn Magn Mater 293:483–496

Prodan E, Radloff C, Halas NJ, Nordlander PA (2003) Hybridization model for the plasmon response of complex nanostructures. Science 302:419–422

Ren G, Hu D, Cheng EWC, Vargas-Reus MA, Reip P, Allaker RP (2009) Characterisation of copper oxide nanoparticles for antimicrobial applications. Int J Antimicrob Agents 33:587–590

Riggio C, Calatayud MP, Hoskins C, Pinkernelle J, Sanz B, Torres TE, Ibarra MR, Wang L, Keilhoff G, Goya GF et al (2012) Poly-L-lysine coated magnetic nanoparticles as intracellular actuators for neural guidance. Int J Nanomed 7:1–12

Smolensky ED, Neary MC, Zhou Y, Berquo TS, Pierre VC (2011) Fe_3O_4@organic@Au: core:shell nanocomposites with high saturation magnetism as magnetoplasmonic MRI contrast agents. Chem Commun 47:2149–2151

Sugimoto T, Matijevíc E (1980) Formation of uniform spherical magnetite particles by crystallization from ferrous hydroxide gels. J Colloid Interface Sci 74:227–243

Suh WH, Suslick KS, Stucky GD, Suh YH (2009) Nanotechnology, nanotoxicology and neuroscience. Prog Neurobiol 87:133–170

Thanh NTK, Green LAW (2010) Functionalisation of nanoparticles for biomedical applications. Nano Today 5:213–230

Wang YXJ, Hussain SM, Krestin GP (2001) Superparamagnetic iron oxide contrast agents: physiochemical characteristics and applications in MR imaging. Eur Radiol 11:2319–2684

Wang H, Brandl DW, Nordlander P, Halas NJ (2007) Plasmonic nanostructures: artificial molecules. Acc Chem Res 40: 53–62

Yavuz MS, Cheng Y, Chen J, Cobley CM, Zhang Q, Rycenga M, Xie J, Kim C, Song KH, Schwartz AG, Wang LV, Xia Y (2009) Gold nanocages covered by smart polymers for controlled release with near-infrared light. Nat Mater 8:935–939

Yuan H, Khoury CG, Hawng H, Wilson CM, Grant GA, Vo-Dinh T (2012) Gold nanostars: surfactant-free synthesis, 3D modelling, and two-photon photoluminescence imaging. Nanotechnology 23:075102

Zhang Q, Ge J, Goebl J, Hu Y, Sun Y, Yin Y (2010) Tailored synthesis of superparamagnetic gold nanoshells with tunable optical properties. Adv Mater 22:1905–1909